Giner Maravilla, E.; Belda, R.; Arango-Villegas, C.; Vercher Martínez, A.; Tarancón Caro, JE.; Fuenmayor Fernández, FJ. (2017). Calculation of the critical energy release rate Gc of the cement line in cortical bone combining experimental tests and finite element models. Engineering Fracture Mechanics. 184:168-182. doi:10.1016/j.engfracmech.2017.08.026

Calculation of the critical energy release rate G_c of the cement line in cortical bone combining experimental tests and finite element models

Eugenio Giner*, Ricardo Belda, Camila Arango, Ana Vercher-Martínez, José E. Tarancón, F. Javier Fuenmayor

Centre of Research in Mechanical Engineering - CIIM
Dept. of Mechanical Engineering and Materials
Universitat Politècnica de València, Camino de Vera, 46022 Valencia, Spain.

Abstract

In this work, a procedure is proposed to estimate the critical energy release rate G_c of the so-called cement line in cortical bone tissue. Due to the difficulty of direct experimental estimations, relevant elastic and toughness material properties at bone microscale have been inferred by correlating experimental tests and finite element simulations. In particular, three-point bending tests of ovine cortical bone samples have been performed and modeled by finite elements. The initiation and growth of microcracks in the tested samples are simulated through finite elements using a damage model based on a maximum principal strain criterion, showing a good correlation with the experimental results. It is observed that microcracks evolve mainly along the cement lines and through the interstitial material but without crossing osteons. The numerical model allows the calculation of the cement line critical energy release rate G_c by approximating its definition by finite differences.

*Corresponding author. Tel.: +34-96-3877007 ext. 76218; fax: +34-96-3877629.
Email address: eginerm@mcm.upv.es (Eugenio Giner)

This way, it is possible to estimate this property poorly documented in the literature.
Keywords: Cortical bone, fracture toughness, microcracks, finite element method, cement line

---

1. INTRODUCTION

Modeling the mechanical performance of bone tissue requires knowledge about the elastic and toughness properties of its structural constituents. The highly hierarchical nature of bone [1, 2] makes it necessary to develop multiscale models in which the different scales must be adequately modeled as found in the literature, e.g. [3, 4].

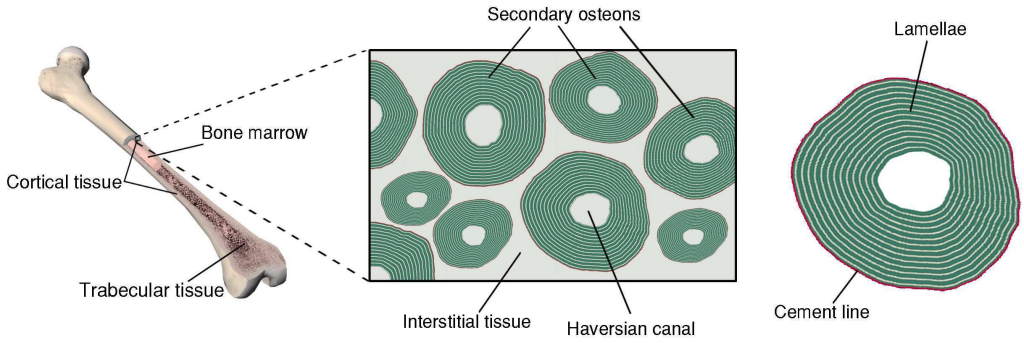

Figure 1: Cortical bone tissue. Main morphological constituents that can be distinguished in a cross section of a long bone.

Fig. 1 shows the basic entities that are modeled in this work and that characterize the morphology of cortical bone tissue. The sketches at the centre and right of Fig. 1 represent the microstructure observed for a cross section of a long bone. The osteon is the basic structural unit of cortical bone and its structure is quite complex at different hierarchical levels [5, 6]. At the submicrostructural level, the osteon is composed of collagen molecules which act as matrix and hydroxyapatite crystals that behave as periodically distributed reinforcements [7]. This periodic structure is grouped into fibrils with different orientations conforming the lamellae, which are concentric layers arranged around the Havers canals that contain blood vessels and nerves

[1, 2, 5, 7], see Fig. 1.

In this work, three-point bending tests of small samples of cortical bone have been performed taken from a cross section of a long bone (sheep tibia). Then, finite element simulations of these samples have been carried out considering the experimental test conditions. The models comprise the existence of multiple osteons, the interstitial tissue that surrounds osteons, and the cement lines that act as the border between osteons and interstitial matrix, formed during bone remodeling processes. In fact, the interstitial matrix corresponds to old, highly mineralized osteons. These constituents are essential for the study of bone fracture at a microstructural level as their role in the bone damage process is not well known yet.

The aim of this work is to estimate some of the elastic and toughness properties of cortical bone tissue at the microstructural level. More specifically, the objective is to estimate the cement line toughness from three-point bending tests and their correlation with numerical simulations of the initiation and growth of microcracks. References to strength properties of the cement line are scarce in the literature, but there is experimental evidence that they play a very important role in the fracture behaviour of cortical bone at microscale, as the cement lines usually act as a weak link diverting crack propagation [8].

O'Brien et al. [9–11] studied the behavior of microcracks in compact bone through experimental tests to get insight into the failure process, showing the importance of the microstructure in the initiation and propagation of microcracks. They distinguished different behavior as a function of the crack length and pointed out the barrier effect of the cement lines for crack

propagation. Short and intermediate microcracks led to crack paths that not penetrate osteons, whereas the crack arrest effect of the cement line is not so evident for long microcracks [10].

Other approaches have been used to model the fracture process in cortical bone tissue. Li et al. [12] performed an experimental study and numerical simulations of fracture processes in bovine femoral cortical bone to characterize fracture toughness, gaining basic understanding of spatial variability and anisotropy of its resistance to fracture. The experimental data was obtained using single-edge-notch-bending specimens of cortical bone tests, while the numerical approach was developed using the extended finite element method (XFEM). They also used this method to investigate the effect of microstructural changes in cortical bone tissue [13].

Guo et al. [14] analyzed the dependence of fracture on the material properties using a simplified model composed of an osteon and the interstitial matrix. Their results suggest that newly formed osteons (with lower stiffness) may toughen cortical bone tissue.

Other authors have simulated material interface behavior at different scales in bone by means of cohesive zone models [4, 15–20]. Lin et al. [18] recently defined a cohesive zone model to define the mechanical behavior at the nano scale of the extrafibrillar matrix in bone. Pereira et al. [19] studied the influence of hydration on the fracture properties of bovine cortical bone at macroscopic scale by carrying out DCB tests. Numerically, they obtained two different cohesive laws under pure mode I loading and, more recently, under mixed-mode I+II loading conditions [20].

Ural and Mischinski [4, 15, 16] used a multiscale approach to study the

influence of the compact bone properties at the micro level on the fracture at the macroscale. They applied a computational fracture mechanics approach based on a cohesive finite element model. At microscale, Ural and Mischinski evaluated 2D finite element models created from human cortical bone microscopy images to determine the influence of cement line properties on the crack propagation path. They concluded that the strength properties of the cement line are relevant for crack deflection. Cox and Yang [17] formulated a cohesive fracture model and analyzed previously published experimental data from human femoral cortical bone. They studied the viability of assuming linear elastic fracture mechanics in cortical bone fracture, claiming that it can only be assumed when cracks are longer than a certain length scale.

In this work, we have carried out three-point bending tests on small samples from a tibia sheep diaphysis, recording the force-displacement responses. The samples have been modeled by the finite element method reproducing the actual sample geometry and the test load conditions, and also the microstructure morphology observed in the micrographs. The finite element model includes different material properties for three constituents: osteons, interstitial matrix and cement lines. The experimental results have enabled the calibration of the response of the whole model and the elastic properties of the constituents considered.

In order to model the crack initiation, we have used a damage criterion based on the maximum principal strain (see Section 3.3), as there are studies that claim that the damage process in bone is strain-controlled [21]. Moreover, the heterogeneity of the bone structure suggests to use a strain-based criterion due to the different stiffness of each component. The mechanical

behavior of bone is often considered as quasi-brittle [5, 22], similar to that observed in other heterogenous materials, such as concrete, mortar, masonry, dentine, biological shells, etc. Damage in quasi-brittle materials is characterized by the development of several microcracks and tortuosity between crack faces, leading to a local loss of stiffness. Eventually these damage phenomena coalesce into a larger crack that is manifested as an evident geometric discontinuity.

In our models, a smeared crack approach has been used to model crack propagation. This approach was proposed in [23] and then used by many researchers in the context of fracture and damage mechanics. The key issue of this approach is that the continuum elements of the finite element model preserve the displacement continuity (it does not allow for the expected displacement discontinuity across crack faces). Instead, the loss of stiffness due to the crack presence is achieved by degradation of the stress-strain constitutive matrices at the element level. The original stiffness of the affected elements is reduced substantially, resembling the crack presence provided the discretization is sufficiently refined. One of the advantages of this procedure is that the same approach is used both for crack initiation and crack propagation. Moreover, it does not need modifications of the mesh topology nor the determination of the crack orientation direction or the elements to be enriched (in the case of the XFEM method). Thus, nonlinear analyses have been performed in this work, considering the degradation of the elastic properties of each microstructural constituent. A similar approach was used by the authors in [24] to model the internal damage in an osteon at the lamellar level.

Using an explicit crack representation as in the XFEM method without consideration of the heterogeneity of the materials may lead to different crack growth paths that cross osteons without following the cement line boundaries. This can be observed in some works in the literature, e.g. [13, 25], and it is not in line with our experimental observations, by which cracks grow along cement line boundaries.

Finally, in this work the strength properties of the microstructural components, i.e. the critical strains associated with cement lines, osteons and interstitial matrix, were estimated using an inverse identification procedure in order to reproduce the damage pattern observed experimentally. This correlation between experimental evidence and the response of the numerical model has also allowed the estimation of the cement line critical strain energy release rate G_c by evaluating the variation of strain energy as the crack grows as detailed in Section 6. The determination of G_c is of interest, since it is an essential property to quantify toughness and characterize cohesive zone models that can simulate the growth of microcracks, like in some of the works commented above.

2. DESCRIPTION OF EXPERIMENTAL TESTS

Three-point bending tests performed on small samples of ovine bone were carried out in this work. First, cross sections were taken from the diaphysis of a sheep tibia in order to obtain sections of cortical tissue of about 1 mm thick, as shown in Fig. 2 left. Then, after removing the periosteum and the associated tissues from endosteum, four samples were obtained from the zones with less curvature. A notch of approximately 0.5 mm wide was generated

in each sample, see Fig. 3. The small notch can also be observed in Fig. 2 right. The samples were kept cold and in appropriate moisture conditions.

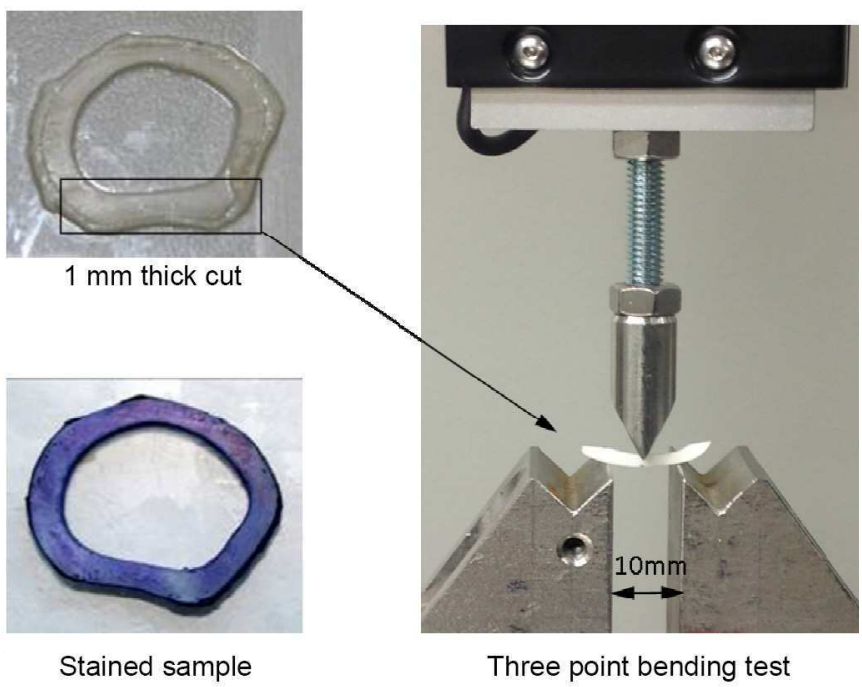

Figure 2: Left: Transversal section of a ovine tibia (before and after staining). Right: Three point bending of the ovine sample.

The three-point bending tests were performed using an electromechanical universal machine. Fig. 2 right shows the testing rig used. Load was applied at a rate of 1 μm/sec, so that tests can be considered quasi-static. The force-displacement response was registered at the load application point for each microsample and the results are presented in Fig. 4, showing a reasonable repeatability. The force-displacement relationship is clearly linear until the applied load reaches a value of about 4.5-5.5 N. From this load level onwards, the damage process begins, reaching high enough stresses in the vicinity of

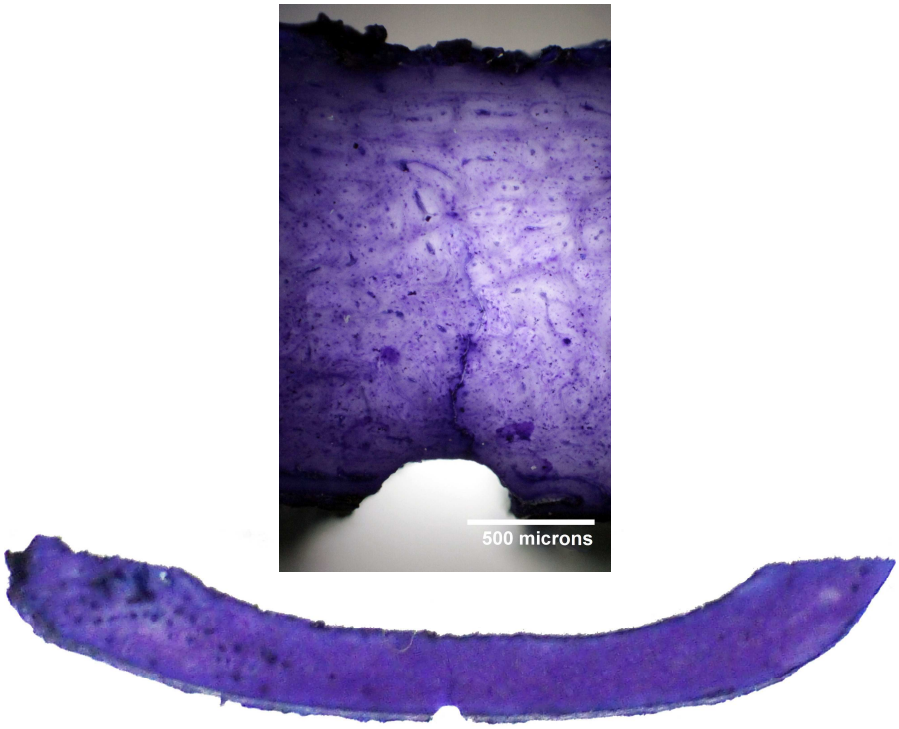

Figure 3: Notched test sample stained after test No. 2.

the notch to promote the growth of microcracks. This results in an evident stiffness loss.

Tests were carried out without reaching complete fracture and avoiding the separation into two halves of the microsamples in order to observe the damage path *a posteriori*. The next step after testing was contrast dyeing (see Fig. 3) and the observation of morphological details (osteons, Havers canals, etc.) to delimit osteons through their cement lines and the generated microcracks (Fig. 5).

For contrast staining of cement lines, the Bain, Impeduglia and Rubin's procedure [26] was followed. It involves samples dehydrating, so it was ap-

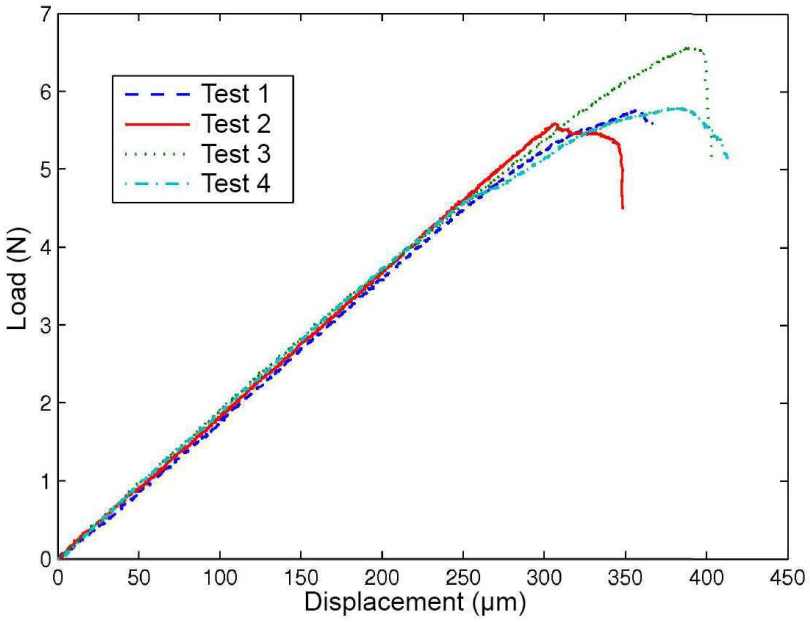

Figure 4: Load-displacement response registered for four tests.

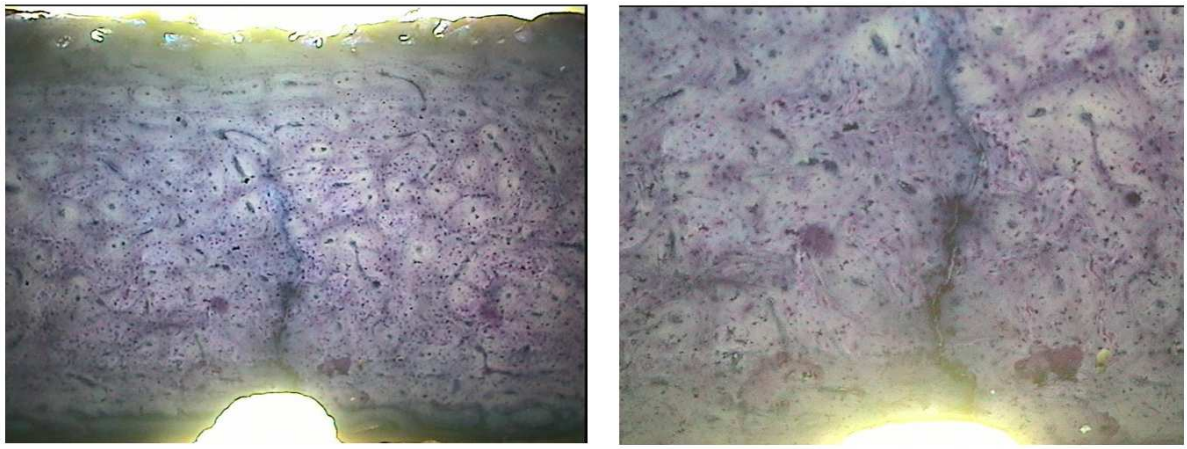

Figure 5: Microsample of test No. 2. Optical microscope view, showing osteons and a microcrack starting from the notch (left 25x, rigth 50x).

plied after testing. The dye is composed of toluidine blue (1 g) in a formic acid solution of 0.1% (100 ml), with pH 2.6. Staining was performed for 20 sec. Subsequently, samples were dehydrated in tert-butyl alcohol (2-methyl-2-propanol) for 30 sec. Care was taken to reduce the staining artifacts, such as dye concentrated remains, by increasing the dehydration time. Finally, a quick xylene rinse was carried out.

Fig. 5 shows the osteon distribution in sample number 2 using optical microscopy. It is observed the dye concentration in the interstitial material, defining in lighter shade the osteons and the Havers canals. The osteon mean diameter is about 100 μm. Some of them have elliptical shapes whose major axis is about 150–200 μm. It is observed the existence of a microcrack evolving primarily along the contours of the osteons, i.e. along the cement lines. The origin of this microcrack is in the area of maximum stress concentration at notch tip.

3. NUMERICAL MODEL

3.1. Geometrical and finite element models

The contours of the osteons and the outer boundaries of the microsamples were defined using the software Plot Digitizer. Determining the osteon boundaries is not a simple task and requires analyst intervention. Only the osteons near the notch and the microcrack propagation zone were segmented, see Fig. 6. For each geometric contour, splines were used to define the cement lines location and the Havers canals. The cement line thickness is considered to be 1 μm [8]. The splines were generated from an Abaqus script in Python. It was deemed not relevant to include further details far from this

area, as regards the mechanical behaviour. These far regions were considered homogeneous with a set of equivalent elastic properties for modelling purposes.

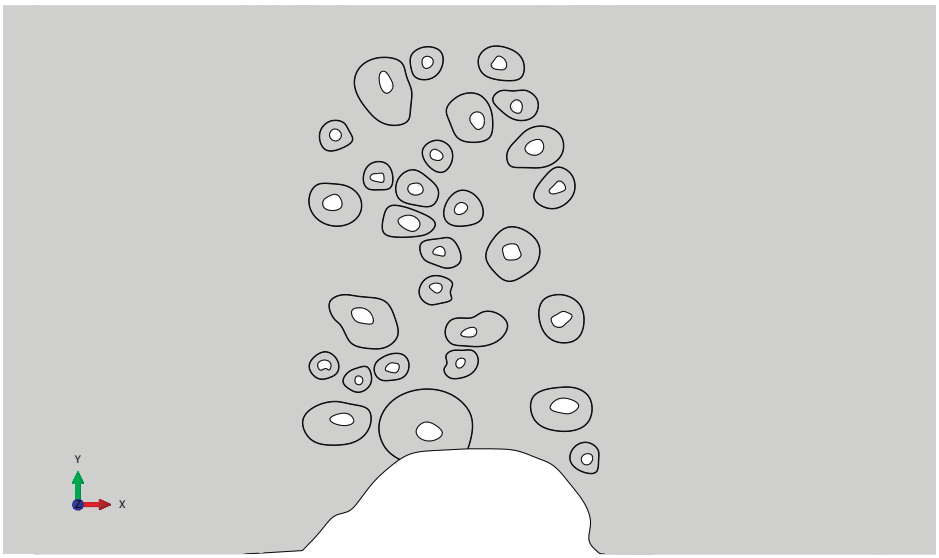

Figure 6: One of the geometrical models with osteons, cement lines and Haversian canals segmented in the vicinity of the notch tip and the region of potential microcrack propagation.

The numerical model was generated in Abaqus. Fig. 7 shows the mesh of the microsample No. 2, composed of 148732 nodes and 148326 triangular and quadrilateral elements (CPS3 and CPS4 in Abaqus). It has been assumed a plane stress condition, due to the small thickness of the microsamples (about 1 mm thick). It can be noticed a high degree of discretization in the region of interest, with element sizes of about 1 μm. In the detail of Fig. 7, the elements of the cement lines are shown in red. The boundary conditions and the applied load are also sketched.

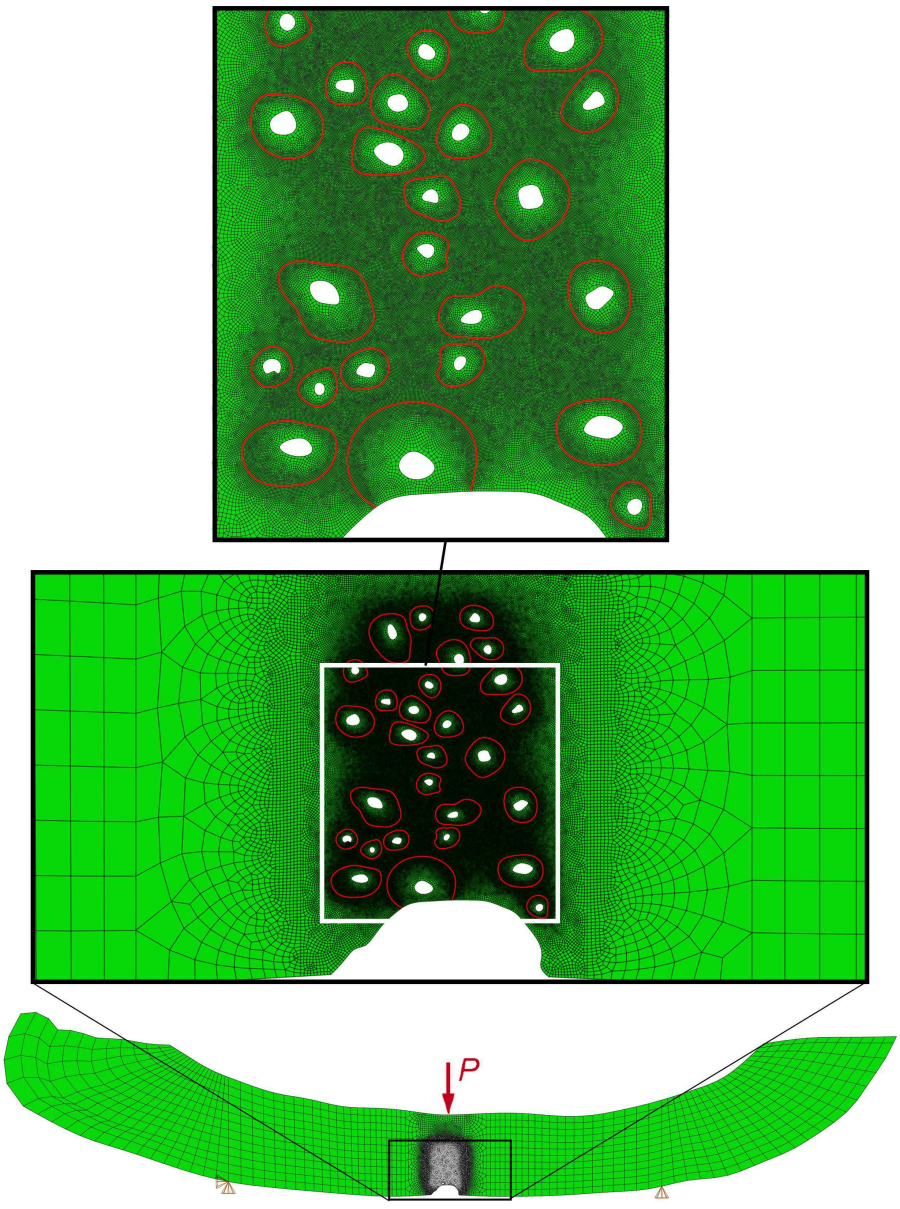

Figure 7: Model mesh showing the boundary conditions and the applied load. The detailed view shows the discretization near the osteon contours. Cement line elements are shown in red.

3.2. Elastic properties

Three different entities are considered in the model: osteons, interstitial matrix and cement lines. It is known that bone tissue presents a significant degree of anisotropy. However, there are not major differences in the transverse plane under study, so the three materials are assumed to be transversely isotropic. A review of the elastic and strength properties can be found in [27]. Initially, we assumed the elastic properties for these three entities in accordance to the literature and previous works, as described below.

Osteon. The value of the stiffness associated to the osteon tissue can vary largely [2, 28] depending on the donor, site, humidity conditions, radial, axial or circumferential direction and even specimen size [28]. One approach is to follow one of our previous works [29], by which a representative element volume of lamellar tissue is homogenized to obtain equivalent elastic properties. According to the five-layer lamellar structure proposed by Weiner et al. [30], which is widely accepted, in [29] the lamellar tissue constitutive matrix is calculated, grouping the five sublayers into the so-called thin lamella and thick lamella (0.8 μm and 2.4 μm thick, respectively).

Following some authors [31, 32], we consider a collagen elastic modulus of $E_{\text{collagen}} = 1.2$ GPa and the homogenization procedure given by Vercher et al. [29] yielding a homogenised value of 3.2 GPa for the osteon stiffness in the transverse direction and 0.3 for the Poisson's ratio. When the collagen elastic modulus is taken as $E_{\text{collagen}} = 5$ GPa, as proposed in [33], the same procedure leads to a homogenised value of 11.2 GPa for the osteon stiffness in the transverse direction, which is clearly greater than the previous value.

Although the theoretical value of 11.2 GPa in the transverse direction is

in line with the widely accepted values for large specimens of cortical bone of 15-18 GPa [28], significantly lower values are obtained when testing microsamples of cortical bone in this latter reference. Thus, for iliac crest cortical tissue of human donors, Kuhn et al. [28] obtained a range for the elastic modulus between 1.19 and 11.25 GPa, with a mean modulus of 4.9 GPa. Note the wide range of variation that can be observed even for the same type of bone, also confirmed by other references cited therein. Ascenzi and Bonucci [34] tested portions of human osteons, obtaining values ranging from 4.81 to 12.9 GPa. We remark that these values are in the longitudinal direction of the osteon and in our work we are interested in the transverse value which is expected to be significantly lower. Kuhn et al. [28] also emphasize the importance of the size effect, stating that there is a decreasing modulus with decreasing specimen size (see this reference for further discussion on this effect).

Regarding the properties of ovine cortical bone, a experimental study is presented in [35] to measure the elastic modulus of different samples of cortical tissue of ovine tibia (the same type of bone used in the present work). The study also includes the measurement in different directions. Thus, values in the longitudinal direction range from 14 to 21 GPa and from 2.5 to 8 GPa in the radial direction (the direction of interest in this work). No information is reported about the sample size, which as commented above may have further influence.

In view of the uncertainty associated with this value, we initially consider a value of $E_{\text{ost}} = 4$ GPa for the osteon stiffness in the transverse direction and $\nu_{\text{ost}} = 0.3$ as the Poisson's ratio. This value will be calibrated after correlating

the numerical test with the experimental results of our own samples.

Interstitial matrix. It is associated with old osteon segments which have been replaced in the continuous process of bone remodelling [5]. Its elastic properties correspond to a more mineralized tissue than the secondary osteons addressed in the previous paragraph. There is consensus in the literature that the interstitial tissue has a stiffness approximately 10 to 15% greater than the osteons [7, 13]. In this work, we have assumed that the stiffness of the interstitial matrix is 10% higher than the osteons, so E_{inters} = 4.4 GPa and $\nu_{\text{inters}} = 0.3$.

Cement line. It can be considered as the interface between the osteon and the interstitial matrix. Compared to lamellar areas, it is very thin (about 1 μm) and its composition is still a topic discussed in the literature. In Burr et al. [8] an analysis of the constituents of the cement line is made and the authors suggest that it is a region with reduced mineralization. This composition is consistent with the hypothesis that the cement line behaves as a relatively weak interface between osteons and interstitial matrix. The low strength of cement lines promotes the crack initiation and propagation, limiting their growth within the interstitial matrix. Similarly, Nobakhti et al. [36] analyse the behavior of the cement line in cortical tissue using a three dimensional model and claim that strains increase at the interfaces for the case of bending. These authors consider that $E_{\text{cl}} = 0.089$ GPa and $\nu_{\text{cl}} = 0.3$. However, in this work we assume that $E_{\text{cl}} = 3.3$ GPa and $\nu_{\text{cl}} = 0.3$, following Ascenzi et al. [37]. Other authors assume even greater stiffness values. For example, Prendergast and Huiskes [38] report $E_{\text{cl}} = 6.0$ GPa, $\nu_{\text{cl}} = 0.25$ and Li et al. [13] $E_{\text{cl}} = 9.6$ GPa, $\nu_{\text{cl}} = 0.3$.

The elastic material properties initially considered for each of the three constituents are summarized in Table 1.

Table 1: Elastic material properties considered initially in the numerical model.

Component	Young's modulus [GPa]	Poisson's ratio
Osteon	4.0	0.3
Interstitial matrix	4.4	0.3
Cement line	3.3	0.3

3.3. Damage modeling

In this work, cortical bone damage is modeled as the degradation of its mechanical properties when critical values are reached. This is accomplished using an Abaqus user's subroutine, whereby a material degradation is introduced to describe the progressive loss of stiffness due to the propagation and coalescence of microcracks, microvoids and similar defects, typical of a continuum damage approach. These changes in the microstructure lead to a material stiffness degradation observed in the macroscale [39]. It has been reported that bone failure process is controlled by strains [21] and since bone structure is highly hierarchical [5, 6] different critical damage strains are proposed for each component.

In a quasi-static regime, the constitutive equation of elasticity modified by a damage mechanics degradation is expressed as follows [40]:

$$\sigma_{ij} = (1 - D)C_{ijkl}\varepsilon_{kl} \tag{1}$$

where D is the damage variable, σ_{ij}, ε_{kl} are the stress and strain tensors and C_{ijkl} is the constitutive elastic tensor.

The implemented Abaqus user's subroutine is a function of a state variable f, which corresponds to the damage criterion. It has been chosen to depend on the principal maximum strain, see Eq. 2:

$$f = \frac{\varepsilon_{p_{\max},i}}{\varepsilon_i^{\mathrm{c}}} \tag{2}$$

where $\varepsilon_{p_{\max},i}$ is the current maximum principal strain and $\varepsilon_i^{\mathrm{c}}$ is the critical damage strain for each constituent i (osteon, interstitial matrix and cement line).

When the critical strain values are reached ($f \geq 1$), the damage variable changes from undamaged to damaged and degradation of the material stiffness is set to 1% of the initial stiffness. This way, the loss of stiffness due to distributed, smeared microcracks is modelled [39]. Since this procedure is implemented in a FE analysis, it is mesh and step dependent, so a sensitivity analysis has been carried out with respect to these two parameters. The mesh dependency of this procedure in certain problems is well known, as discussed e.g. in [41]. A sufficiently refined mesh has been generated in the zones where damage is expected to initiate and the substeps have been chosen small enough to get a convergent solution.

We note in passing that other authors in the literature have opted for an explicit crack approach to model the existence of microcracks in cortical bone at the microscale. This is the case found in [13, 25]. In such an explicit approach, the displacement discontinuity between crack faces is explicitly modelled, either using a classical FE analysis (by which the element sides match the crack faces) or using the extended finite element method XFEM (by which the crack location does not need to conform to the element sides). Despite the advantages of the XFEM approach, a typical implementation

of the XFEM method, as the one available in the commercial code Abaqus, poses difficulties when applied to heterogeneous materials. In fact, results reported in [13, 25] lead to crack paths that cross osteons, differing from our experimental evidence. Therefore, in this work we have followed a smeared crack approach described above to model microcracks in cortical bone tissue.

4. CALIBRATION OF THE NUMERICAL MODEL WITH EXPERIMENTAL RESULTS

4.1. Force-displacement response

The numerical analysis of the microsample models should reproduce the linear range of the force-displacement response obtained experimentally, see Fig. 4. Preliminar analysis using the stiffness properties proposed in Subsection 3.2 show that the response of the numerical model is stiffer than the experimental measures (about 4.5 times stiffer). Since the shape and dimensions of the microsamples have been modeled accurately and the boundary conditions are simple, the excessively rigid behaviour of the numerical model must be ascribed to the stiffness material properties input in the model. These should be modified in consequence to calibrate the model and reproduce the actual behaviour.

After dividing by the calibrating scale factor (approximately 4.7), the calibrated stiffnesses for each region that lead to the observed experimental behaviour are: $E_{\text{ost,cal}} = 0.86$ GPa, $E_{\text{inters,cal}} = 0.95$ GPa and $E_{\text{cl,cal}} = 0.57$ GPa. This way, the simulation response matches the experimental behaviour in the linear elastic range, see Fig. 8.

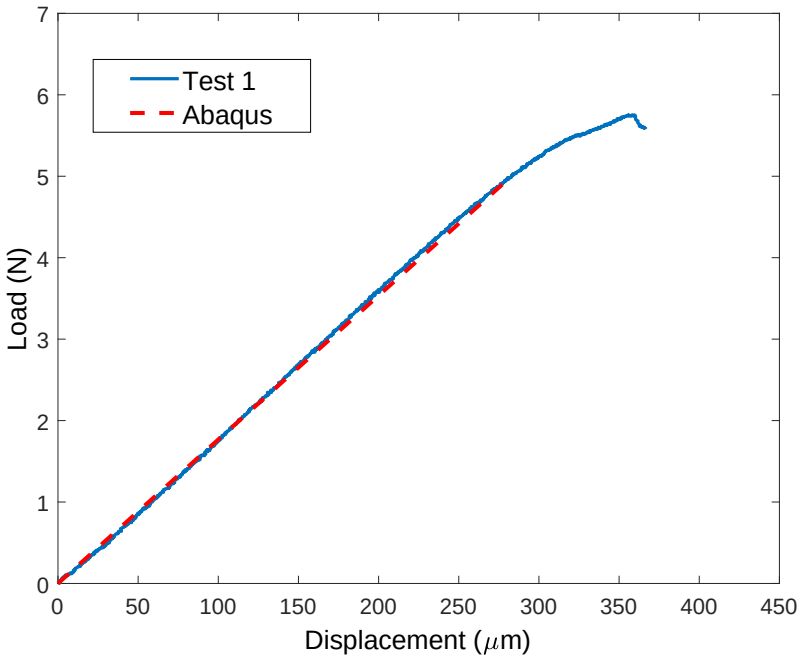

Figure 8: Force-displacement response obtained using the calibrated FE model and the experimental record for test No. 1.

The calibrated values are relatively close (except for the interstitial matrix) to the values provided by Nobakhti et al. [36] in his recent work in which small microsamples of cortical bone are tested. In [36], they refer an osteon stiffness of $E_{\text{ost,transversal}} = 0.15$ GPa, $E_{\text{ost,longitudinal}} = 5$ GPa, $E_{\text{inters}} = 13.7$ GPa and $E_{\text{cl}} = 0.088$ GPa, which for $E_{\text{ost,transversal}}$ and E_{cl} are even less than those estimated here after calibration. Once more, this shows the great dispersion of mechanical properties found in the literature, as discussed in Section 3.2.

4.2. Critical strain for each component at the microscale

Fig. 9 shows the in-plane maximum principal strain contour reached after applying a growing force up to 5 N for microsample 4. As expected, the maximum principal strain value is reached at the cement line closest to the notch, i.e. the zone most prone to failure, as it has been observed experimentally. At the failure load, the maximum principal strains in the cement lines (in red) are slightly greater than 0.07, so the critical damage strain for the cement line is assumed to be about this value.

In order to determine the critical damage strain values, an iterative procedure has been carried out, analyzing the damage pattern obtained according to the critical parameters until the experimental crack path is reproduced approximately. Thus, by inverse analysis, it is possible to determine the critical damage parameters for each of the three constituents considered in the numerical model. The estimation of the critical strain for each component is shown in Table 2 for the two tests analyzed. For both cases, the estimated critical values are similar even though they come from different models with a different morphology at the microscale.

Table 2: Critical strain for each constituent.

ε_i^c	Osteon	Cement line	Interstitial matrix
Test 2	0.12	0.07	0.07
Test 4	0.12	0.08	0.06

4.3. Crack growth simulation

Following the above procedure, the damaged elements form a smeared crack pattern in good agreement with the experimental crack paths, see

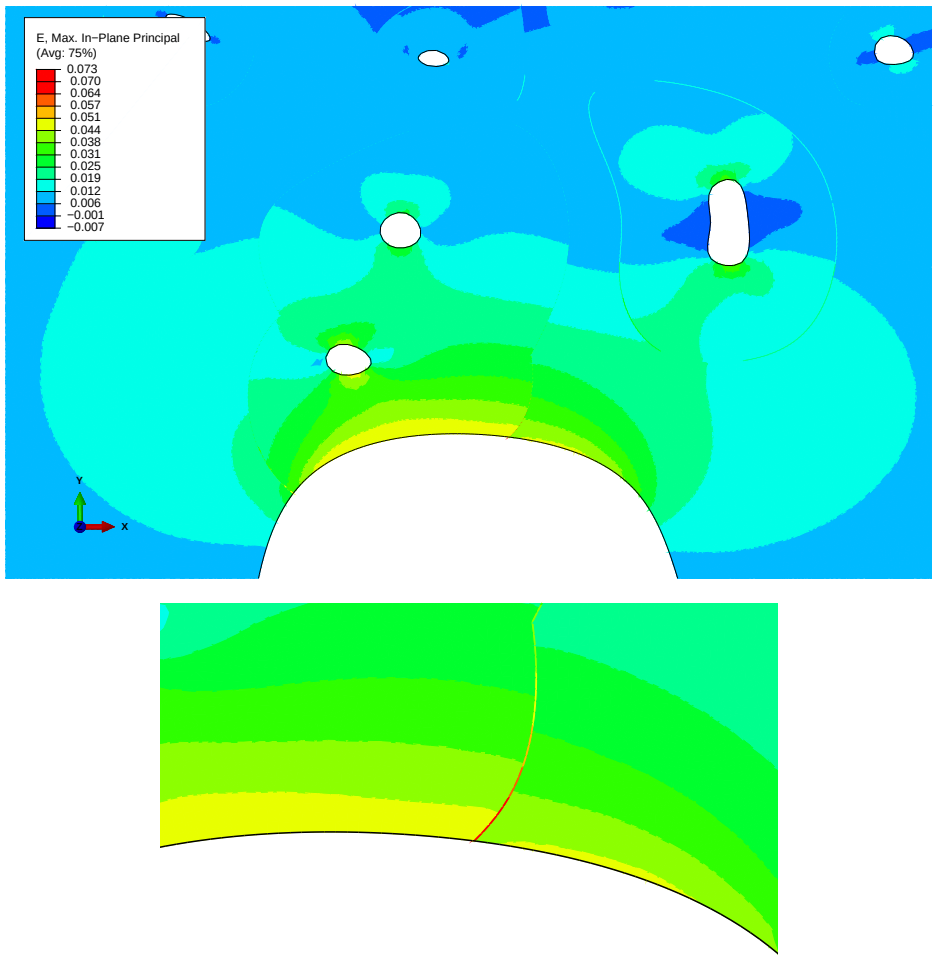

Figure 9: Maximum principal strain in the region near the notch of microsample No. 4.

Figs. 10 and 11. For both samples, microcracks initiate at the closest cement line to the notch, i.e. where cement line strains are the greatest. Furthermore, it is clearly observed how microcracks evolve along the cement lines, through the interstitial matrix and without crossing the osteons, which is in agreement with experimental observations. This is in line with one of the claimed functionalities of bone microstructure, by which cement lines act as

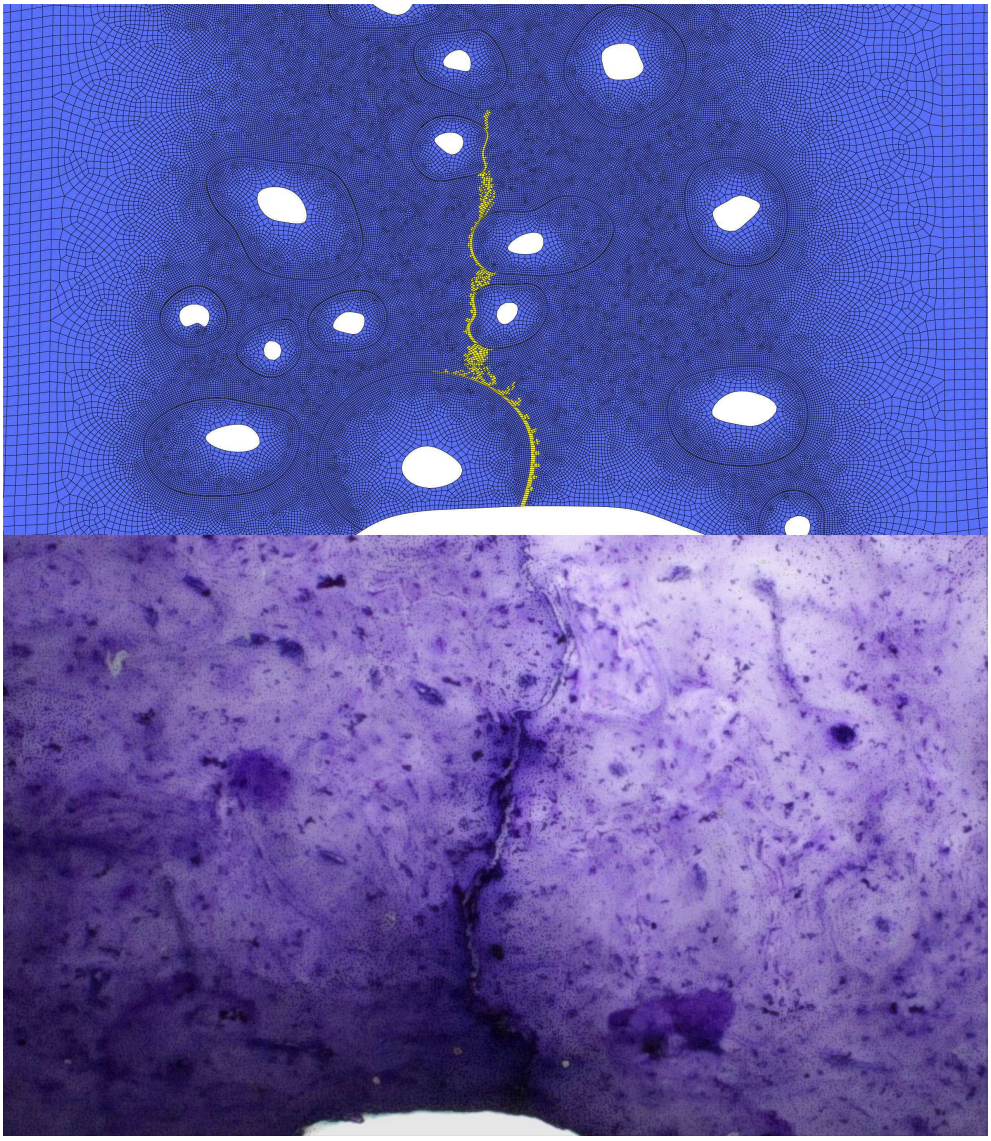

Figure 10: Crack path comparison between simulation and experimental results for sample 2.

a protective component of the haversian system.

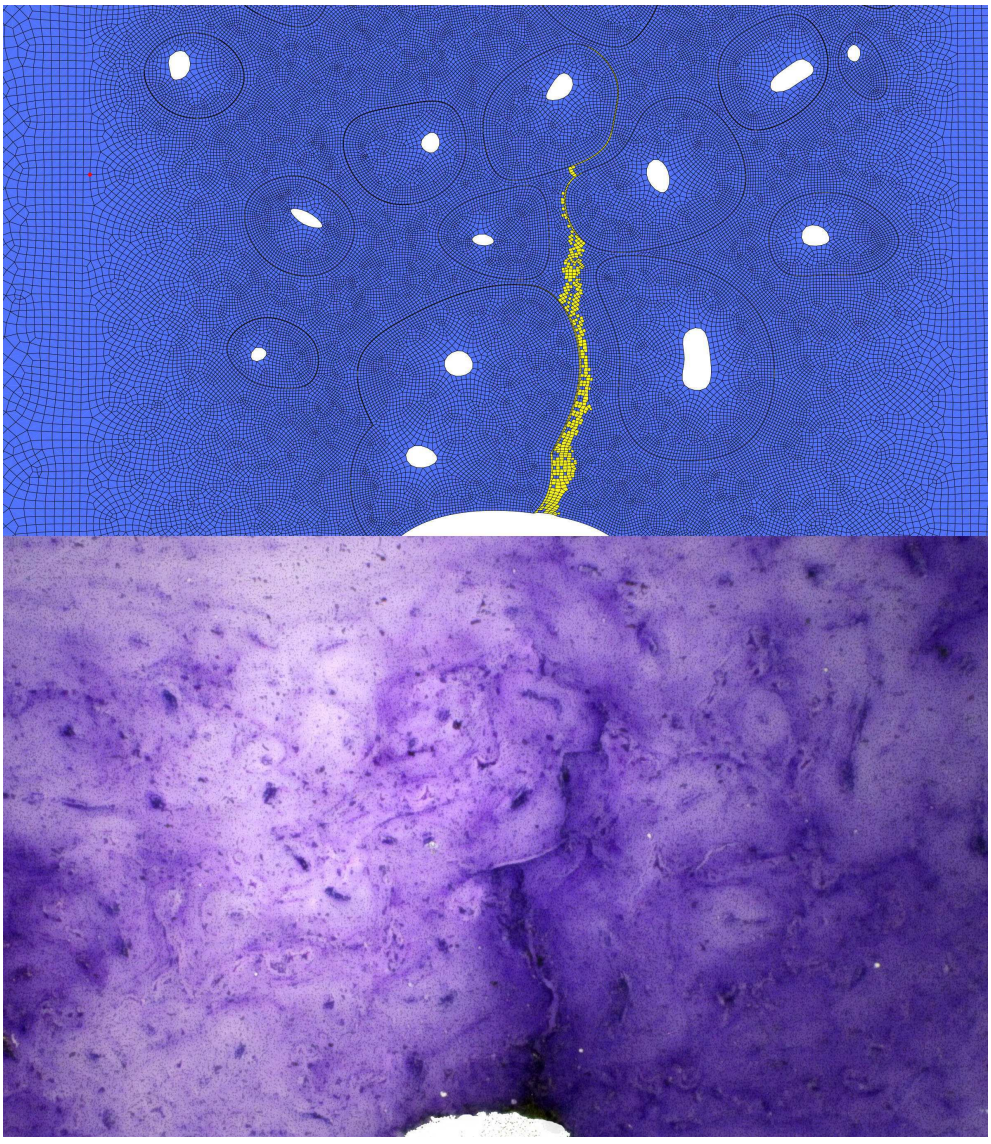

Figure 11: Crack path comparison between simulation and experimental results for sample 4.

5. DISCUSSION

The evolution of microcracks along cement lines has been observed by many investigators. The thorough study by Burr et al. [8] evidences that cement lines play an important role in the fracture behaviour at microscale, as they are observed to divert crack propagation. Some investigators have suggested that cement lines are not crossed by collagen fibers and represent the weakest link within the cortical bone tissue [42, 43]. This approach is consistent with the situation observed experimentally, by which microcracks tend to follow cement lines rather than crossing osteons [44]. As shown in the previous section, this is also the case of the experiments carried out in this work. In Kennedy et al. [45], microcracks are analized in the remodeling process as a function of its length, showing different behaviors. Short and intermediate or long cracks propagate through the interstitial matrix until reaching cement lines, but longer cracks tend to get arrested at cement lines of new osteons rather than at old ones [45].

Other results in the literature show crack paths crossing osteons when studying fracture in cortical bone tissue [9–11, 46]. Chan et al. [46] studied crack propagation in two cortical bone human femur specimens and the influence of the donor's age. Within young specimens, microcracks mainly propagate through the cement lines and the interstitial matrix, but rarely crossing osteons. Cracks frequently get arrested or deflect when they encounter an osteon and follow its cement line. However, some osteons are not capable to deflect cracks and they penetrate through the lamellar tissue, as in the case of old donor specimens [46]. These authors suggest that the different behavior observed depends on factors such as different mineralization states,

the degree of collagen crosslink density and differences in the remodelling process [46]. These factors can lead to different crack behavior.

In general, there is agreement that short and intermediate microcracks lead to crack paths that not penetrate osteons, as observed in the experiments performed in this work, and that the crack arrest effect is less evident for long microcracks, as commented in [10]. There is consensus that the mechanical role of cement line needs still of further investigations. The wide dispersion of mechanical properties at microscale for stiffness and strength of the different bone constituents, as discussed in Section 3.2, makes this type of studies even more complicated. In next section, we propose a procedure to estimate the critical energy release rate of cement line using the force-displacement experimental results and the above numerical simulations.

6. ESTIMATION OF THE CRITICAL ENERGY RELEASE RATE G_c FOR THE CEMENT LINE

The objective of this section is to estimate the critical energy release rate G_c associated with the cement lines using FE results. This property is considered of special relevance and it is useful, for example, to characterize cohesive zone models (CZM) that need a knowledge of the critical energy of fracture. In fact, this property is poorly documented in the literature with high scattered values and, in this work, we propose a procedure to estimate this material property.

First, the numerical models are calibrated for the experimental damage load, leading to an acceptable path prediction along cement lines. Then, we recall the definition of the strain energy release rate G:

$$G = -\frac{\mathrm{d}\Pi}{\mathrm{d}A} \tag{3}$$

where Π is the total potential energy of the system and A is the crack area. It is easy to prove that, when quasi-static crack propagation occurs (either at constant load, constant displacement or variation of both) and assuming a material with a linear elastic response, Eq. 3 can be rewritten in terms of the variation of the elastic strain energy of the system U as:

$$G = \left| \frac{\mathrm{d}U}{\mathrm{d}A} \right| \tag{4}$$

Assuming a two-dimensional problem with crack length a and thickness t, Eq. 4 can be approximated by a finite difference approach as follows:

$$G = \frac{1}{t} \lim_{\Delta a \to 0} \left| \frac{\Delta U}{\Delta a} \right| = \frac{1}{t} \lim_{\Delta a \to 0} \left| \frac{U_{i+1} - U_i}{\Delta a} \right| \tag{5}$$

It is possible to estimate the critical value G_c when a crack grows along the cement line about the failure load value detected experimentally, performing a FE simulation with small enough time increments. During the critical time increments, a certain number of elements change from a non-damaged state to a damaged state. The length of this set of elements can be identified with Δa, i.e. the crack growth that occurs between two consecutive time increments when the critical load is reached. The numerical value of the elastic strain energy U_i for each step is provided by the FE solution at each load increment. By substitution into Eq. 5 for the critical load increments (for which propagation of damaged elements is observed), an estimation of G_c can be obtained.

Fig. 12 represents the first substeps at which failure of the cement line near the notch is produced. This occurs when the experimental critical load is reached and the force-displacement response becomes nonlinear due to damage and microcracks initiation. The loading process was divided into small time increments (1000 substeps), so the load variation between successive substeps is very small.

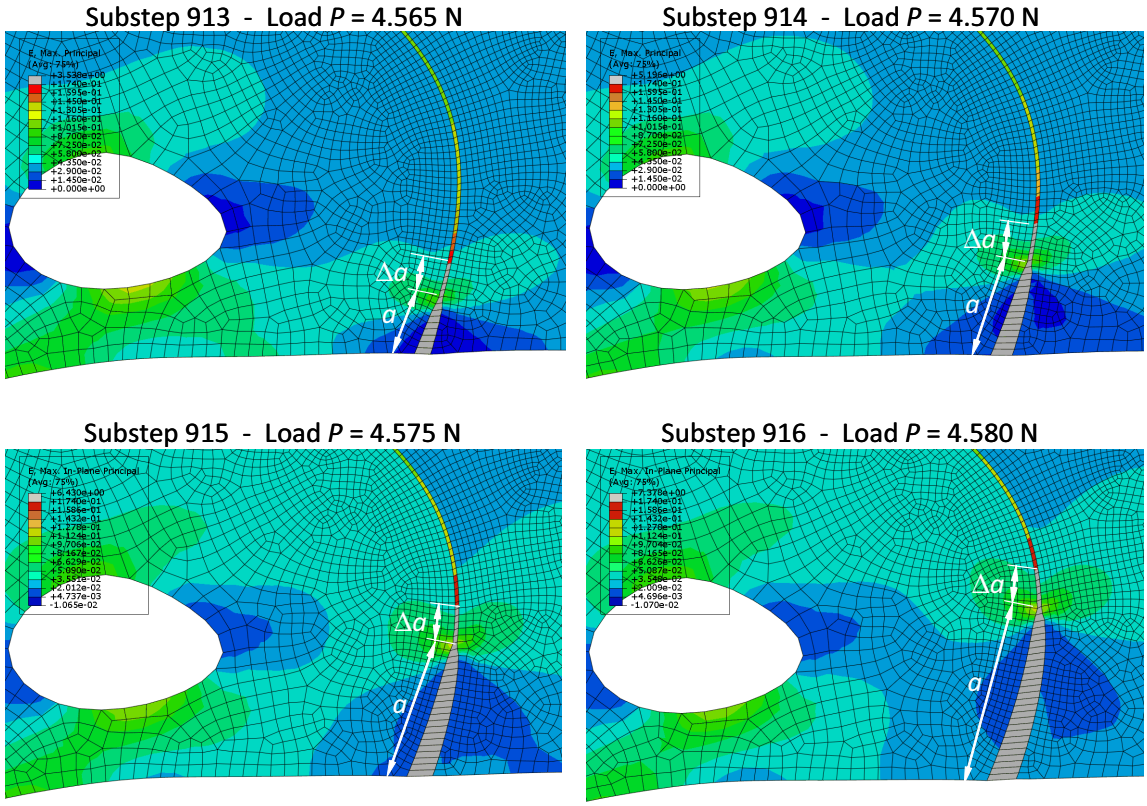

Figure 12: G_c calculation for the cement line.

Crack growth is observed in Fig. 12, where similar crack increment lengths Δa are found between substeps for this load level. The energy supplied to

the system as an external force work causes a crack growth of Δa equivalent to 5-6 elements, requiring an energy consumption to generate new crack faces that is similar in each substep and that can be related to the critical energy release rate G_c of the failed material. Table 3 shows the strain energy of the system extracted from the FE analysis for each of the six substeps analyzed in this section.

Table 3: Elastic strain energy for each load substep.

Substep i	Load [N]	U_i [10^{-6}Nm]
913	4.565	553.86
914	4.570	555.37
915	4.575	556.91
916	4.580	558.48
917	4.585	560.07
918	4.590	561.88

Table 4 shows the estimated values of G_c for the above six successive load increments using Eq. (5), having considered a sample thickness of $t = 1$ mm.

Since the value of the applied load corresponds to the critical load associated with the beginning of non-linear behavior, the values of G can be identified as the critical strain energy release rate of the cement line $G_{c,cl}$. The average value of $G_{c,cl}$ is 162.9 N/m. This value is of the order of the value provided by Li et al. [13], who refer that G_c for the cement line is 146 N/m, although the bone type is not indicated and their result is based on other works.

Regarding the method for estimating G_c, we would like to point out its

Table 4: Estimation of the cement line critical energy release rate G_c for each substep using Eq. (5). Sample thickness is 1 mm.

Substep i	Δa [10^{-6}m]	$G = G_c$ [N/m]
913-914	9.853	152.8
914-915	9.853	157.0
915-916	9.853	159.5
916-917	9.852	160.9
917-918	9.851	184.2

simplicity of application and its global character, so that the crack does not need to be explicitly defined. It can be applied to interfaces between heterogeneous materials, as presented here, which otherwise would complicate the application of other advanced techniques, such as the J-integral. Moreover, it does not involve the calculation of local displacements or stresses in the vicinity of the crack tip, where these fields are affected by a large discretization error.

One of the limitations of the method proposed for estimating G_c is that it does not allow the separation between mode I and mode II contributions. In principle, with the appropriate choice of the testing configuration, one can obtain the desired crack opening mode. In our work, the computed value of G_c corresponds in practice to G_{Ic} since the crack evolves almost normal to the maximum principal stresses due to bending in the neighborhood of a notch tip. Of course, when the cement line follows a contour not normal to the maximum principal stress, then a mode II contribution exists. Due to the geometrical configuration of the cement line and specimen used in

this section, we provide an approximation to G_{Ic} through the crack growth increments used in the computation of G.

7. CONCLUSIONS

Three-point bending tests have been performed on cortical bone tissue samples and their behaviour correlated by finite element models. The geometry of the samples and the morphology of the osteons in the region of interest have been taken into account in the numerical model, distinguishing between three constituents at the micro level: osteons, interstitial matrix and cement lines. The experimentally recorded force-displacement response enabled the calibration of the elastic and strength properties of the constituents considered. The calibrated elastic properties are in the range of other values reported in the literature, where a wide range of values have been found. The critical damage strain was also calibrated for each constituent (osteon, cement line and interstitial matrix), enabling the simulation of the damage initiation and crack growth pattern using a smeared crack approach. Both experimental tests and numerical simulations are in good agreement. Results show that microcracks in cortical bone tissue tend to evolve mainly along the cement lines, crossing the interstitial matrix, and hence cement lines act as a protective element of the haversian system.

Furthermore, the critical energy release rate of the cement line $G_{\mathrm{c,cl}}$ has been estimated using a finite difference approximation of the variation of the strain energy of the system (measured from the calibrated FE models) as the crack advances through the cement line. This property is relevant and can be very useful to formulate other models, e.g. cohesive zone models

(CZM) of the interface. This work sets a procedure that can be applied in further experimental tests in order to estimate strength properties of bone constituents at the micro scale.

ACKNOWLEDGEMENTS

The authors wish to thank the Ministerio de Economía y Competitividad for the support received in the framework of the project DPI2013-46641-R and to the Generalitat Valenciana, Programme PROMETEO 2016/007. The authors also thank Dr. José Luis Peris, from Instituto de Biomecánica de Valencia (IBV) and Carlos Tudela Desantes for their collaboration within the context of the project.

REFERENCES

References

[1] Currey JD. The structure and mechanics of bone. J Mater Sci 2012;47:41–54.

[2] Rho JY, Kuhn-Spearing L, Zioupos P. Mechanical properties and the hierarchical structure of bone. Med Eng Phys 1998;20:92-102.

[3] Burczynski T, Kus W, Brodacka A. Multiscale modeling of osseous tissues. J Theor Applied Mech 2010;48(4):855–70.

[4] Ural A, Mischinski S. Multiscale modeling of bone fracture using cohesive finite elements. Engng Fract Mech 2013;103:141–52.

[5] Cowin SC. Bone Mechanics Handbook. Boca Ratón, Florida:CRC Press;2001.

[6] Taylor D, Hazenberg JG, Lee TC. Living with cracks: Damage and repair in human bone. Nature Mater 2007;6:263–68.

[7] Rho JY, Currey JD, Zioupos P, Pharr GM. The anisotropic Young's modulus of equine secondary osteons and interstitial bone determined by nanoindentation. J Exper Biology 2001;204:1775–81.

[8] Burr DB, Schaffler MB, Frederickson RG. Composition of the cement line and its possible mechanical role as a local interface in human compact bone. J Biomech 1988;21:939–45.

[9] O'Brien FJ, Taylor D, Lee TC. Microcrack accumulation at different intervals during fatigue testing of compact bone. J Biomech 2003;36:973–80.

[10] O'Brien FJ, Taylor D, Lee TC. The effect of bone microstructure on the initiation and growth of microcracks. J Orthop Res 2005;23:475–80.

[11] O'Brien FJ, Hardiman DA, Hazenberg JG, Mercy MV, Moshin S, Taylor D, Lee TC. The behavior of microcracks in compact bone. Eur J Morphol 2005;42(1-2):71–9.

[12] Li S, Abdel-Wahab A, Silberschmidt VV. Analysis of fracture processes in cortical bone tissue. Engng Fract Mech 2013;110:448–58.

[13] Li S, Abdel-Wahab A, Demirci E, Silberschmidt VV. Fracture process

in cortical bone: X-FEM analysis of microstructured models. Int J Fract 2013;184:43–55.

[14] Guo XE, Li LC, Goldstein SA. Micromechanics of osteonal cortical bone fracture. Trans ASME J Appl Mech 1998;120:112–17.

[15] Mischinski S, Ural A. Finite element modeling of microcrack growth in cortical bone. J Appl Mech-ASME 2011;78(4):No.041016.

[16] Mischinski S, Ural A. Interaction of microstructure and microcrack growth in cortical bone: a finite element study. Comput Meth Biomech Biomed Engng 2013;16(1):81–94.

[17] Cox BN, Yang Q. Cohesive zone models of localization and fracture in bone. Engng Fract Mech 2007;74:1079–92.

[18] Lin L, Wang X, Zeng X. An improved interfacial bonding model for material interface modeling. Engng Fract Mech 2017;169:276–91.

[19] Pereira FAM, Morais JJL, de Moura MFSF, Dourado N, Dias MIR. Evaluation of bone cohesive laws using an inverse method applied to the DCB test. Engng Fract Mech 2012;96:724–36.

[20] Pereira FAM, de Moura MFSF, Dourado N, Morais JJL, Silva FGA, Dias MIR. Bone fracture characterization under mixed-mode I+II loading using the MMB test. Engng Fract Mech 2016;166:151–63.

[21] Nalla RK, Kinney JH, Ritchie RO. Mechanistic fracture criteria for the failure of human cortical bone. Nat Mater 2003;2:164–68.

[22] Pietruszcak S, Gdela K, Webber CE, Inglis D. On the assessment of brittle-elastic cortical bone fracture in the distal radius. Engng Fract Mech 2007;74:1917–27.

[23] Rashid YR. Analysis of reinforced concrete pressure vessels. Nucl Engng & Design 1968;7:334–44.

[24] Giner E, Arango C, Vercher A, Fuenmayor FJ. Numerical modelling of the mechanical behaviour of an osteon with microcracks. J Mech Behav Biomed Mat 2014;37: 109–24.

[25] Budyn E, Hoc T, Jonvaux J. Fracture strength assessment and aging signs detection in human cortical bone using an X-FEM multiple scale approach. Comput Mech 2008;42:579-91.

[26] Bain SD, Impeduglia TM, Rubin CT. Cement line staining in undecalcified thin sections of cortical bone. Stain Technol 1990;65:1–5.

[27] Arango C, Giner E, Vercher A, Fuenmayor FJ. Modelado tridimensional del fallo progresivo de la microestructura del hueso cortical mediante elementos finitos. Actas del XXXI Encuentro del Grupo Español de Fractura, San Lorenzo del Escorial 2014.

[28] Kuhn JL, Goldstein SA, Choi K, London M, Feldkamp LA, Matthews LS. Comparison of the trabecular and cortical tissue moduli from human iliac crests. J Orthop Res 1989;7:876–84.

[29] Vercher A, Giner E, Arango C, Tarancón JE, Fuenmayor FJ. Homogenized stiffness matrices for mineralized collagen fibrils and lamellar bone

using unit cell finite element models with periodic boundary conditions. Biomech Model Mechanobiol 2014;13:437–49.

[30] Weiner S, Traub W, Wagner H. Lamellar bone: structure-function relations. J Struct Biol 1999;126:241-55.

[31] Martínez-Reina J, Domínguez J, García-Aznar JM. Effect of porosity and mineral content on the elastic constants of cortical bone: a multiscale approach. Biomech Model Mechanobiol 2011;10:309-22.

[32] Vercher A, Giner E, Arango C, Fuenmayor FJ. Influence of the mineral staggering on the elastic properties of the mineralized collagen fibril in lamellar bone. J Mech Behavior Biomed Mater 2015;42:243-56.

[33] Reisinger AG, Pahr DH, Zysset PK. Elastic anisotropy of bone lamellae as a function of fibril orientation pattern. Biomech Model Mechanobiol 2011;10:67-77.

[34] Ascenzi A, Bonucci E. The tensile properties of single osteons. Anat Rec 1967;158:375–86.

[35] Grant CA, Langton C, Schuetz MA, Epari DR. Determination of the material properties of ovine cortical bone. Poster No. 2226, 57th Orthopaedic Research Society (ORS) Annual Meeting, Long Beach, California 2011.

[36] Nobakhti S, Limbert G, Thurner PJ. Cement lines and interlamellar areas in compact bone as strain amplifiers contributors to elasticity, fracture toughness and mechanotransduction. J Mech Behav Biomed Mat 2014;29:235–51.

[37] Ascenzi MG, Kawas NP, Lutz A, Kardas D, Nackenhorst U, Keyak JH. Individual specific multi scale finite element simulation of cortical bone of human proximal femur. J Comput Phys 2013;244:298–11.

[38] Prendergast PJ, Huiskes R. Microdamage and osteocyte-lacuna strain in bone: a microstructural finite element analysis. J Biomech Engng 1996;118(2):240-46.

[39] Jirásek M. Damage and smeared crack models. In: Hofstetter G and Meschke G, editors. Numerical modeling of concrete cracking, CISM courses and lectures, Wien:Springer; 2011;532:1–49.

[40] Lemaitre J. A continuous damage mechanics model for ductile fracture. J Eng Mater Technol 1985;107:83–9.

[41] Lapczyk I, Hurtado JA. Progressive damage modeling in fiber-reinforced materials. Composites: Part A 2007;38:2333–41.

[42] Evans FG, Bang S. Physical and histological differences between human fibular and femoral compact bone. In: Evans FG, ed. Studies on the Anatomy and Function of Bone and Joints. Springer; 1966 p.142–55.

[43] Maj G, Toajari E. Osservazioni sperimentali sul meccanismo di resistenza del tessuto osseo lamellare compatto alle azioni meccaniche. Chir Org Mov 1937;22:541–57.

[44] Skedros JG, Holme JL, Vajda EG, Bloebaum RD. Cement lines of secondary osteons in human bone are not mineral-deficient: new data in a historical perspective. Anat Rec A Discov Mol Cell Evol Biol 2005;286:781–03.

[45] Kennedy OD, Brennan O, Mauer P, Rackard SM, O'Brien FJ, Taylor D, Lee TC. The effects of increased intracortical remodeling on microcrack behavior in compact bone. Bone 2008;43:889–93.

[46] Chan KS, Chan CK, Nicolella DP. Relating crack-tip deformation to mineralization and fracture resistance in human femur cortical bone. Bone 2009;45:427–34.